Chapter 2

Electron Oscillators in a Cylindrical Cavity

This study of the collective behavior of parametrically pumped electron oscillators is made possible by a cylindrical Penning trap (Fig. 2.1) which is constructed to be the best possible approximation to an ideal microwave cavity. As we shall see, trapped electrons can be used to clearly observe the radiation modes of the cylindrical trap cavity. The observed resonance frequencies correspond extremely well to the familiar eigenfrequencies ν_{mnp} of an ideal cylinder (Fig. 2.2). We can thus classify and identify the electromagnetic standing wave fields in a familiar way as either transverse magnetic or transverse electric modes. With some effort, sections of the cavity walls are made to be the electrodes of a Penning trap. Trapped electrons are thereby localized within well-characterized standing wave fields and the interaction of the electrons with the surrounding radiation field is under precise control.

The familiar eigenfrequencies for a cylindrical microwave cavity of height $2z_0$ and radius ρ_0 (Fig. 2.2) are given by [49]

$$2\pi\nu_{mnp} = c\sqrt{\left(\frac{\chi_{mn}}{\rho_o}\right)^2 + \left(\frac{p\pi}{2z_o}\right)^2}, \tag{2.1}$$

where c is the speed of light. For transverse magnetic modes TM_{mnp}, the χ_{mn} is the nth zero of the mth order Bessel function $J_m(x)$ and $p = 0, 1, 2, \ldots$. For

transverse electric modes TE_{mnp}, the χ_{mn} is the nth zero of the Bessel function derivative $J'_m(x)$ and $p = 1, 2, \ldots$. In both cases, $m = 0, 1, \ldots$ and $n = 1, 2, \ldots$. The electromagnetic fields for each of the standing wave modes are simple analytic functions [49]. Great care was taken to make a cylindrical trap cavity which closely approximates an ideal cylindrical microwave cavity. This makes it possible to thoroughly analyze the interaction of particular cavity radiation modes with a single electron localized in the trap cavity (summarized in Sec. 4.4).

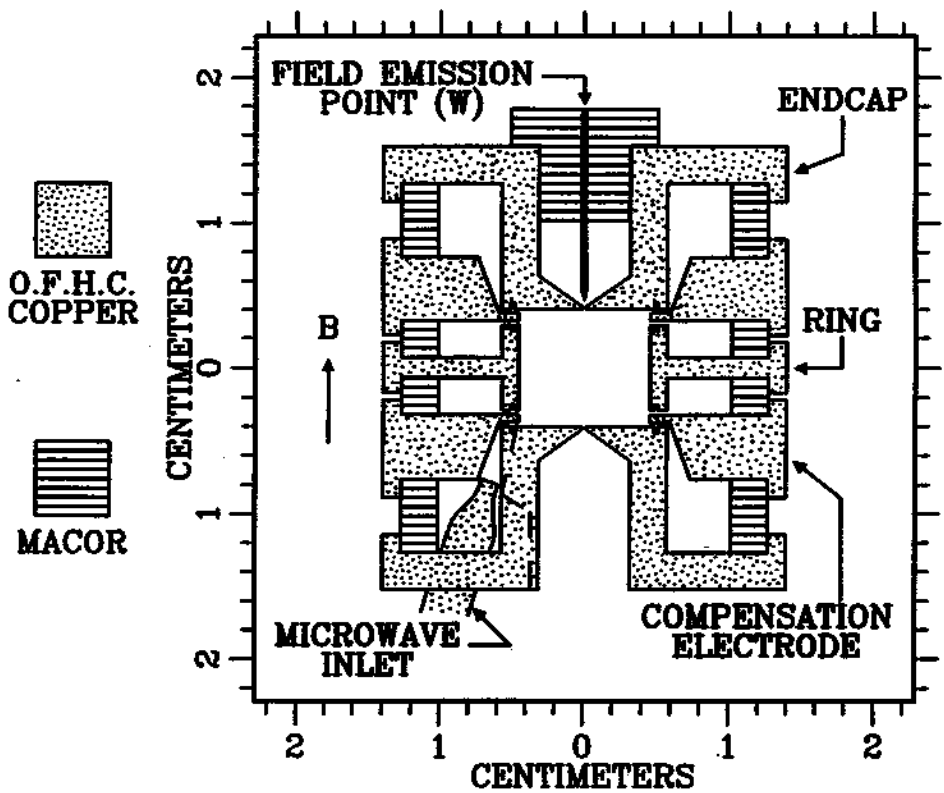

Figure 2.1: Orthogonalized cylindrical trap cavity (to scale with $z_0 = 0.3838(6)$ cm and $\rho_0 = 0.4559(6)$ cm at 4 K). A spatially uniform magnetic field ($\Delta B/B < 10^{-6}$ over $z_0/10$) is along the vertical axis. Choke flanges ($\lambda/4$ at 164 GHz) are incorporated to minimize losses.

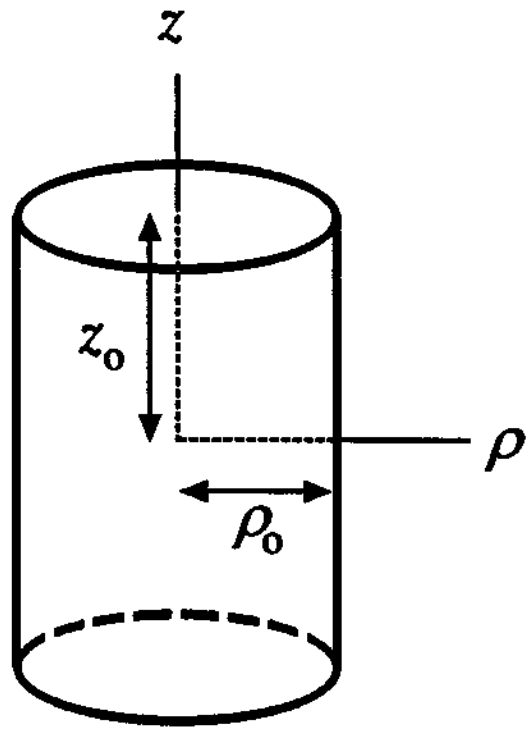

Figure 2.2: Ideal cylindrical cavity.

Of particular interest are the standing wave modes which couple to electron cyclotron motion which is perpendicular to the axis of the cylinder and typically near to it. Such coupling requires an electric field perpendicular to the cylinder axis. This is provided by either TE_{1np} or TM_{1np} standing wave modes, provided that the electron is not localized in an axial standing wave minimum. To illustrate, the transverse electric fields of TE_{1np} modes near the symmetry axis of the cavity are simple sine and cosine functions of the z-coordinate (relative to the center of the cavity). The quantum number p indicates the number of standing wave maxima (anti-nodes) which fit between the two endcaps. For modes with odd p,

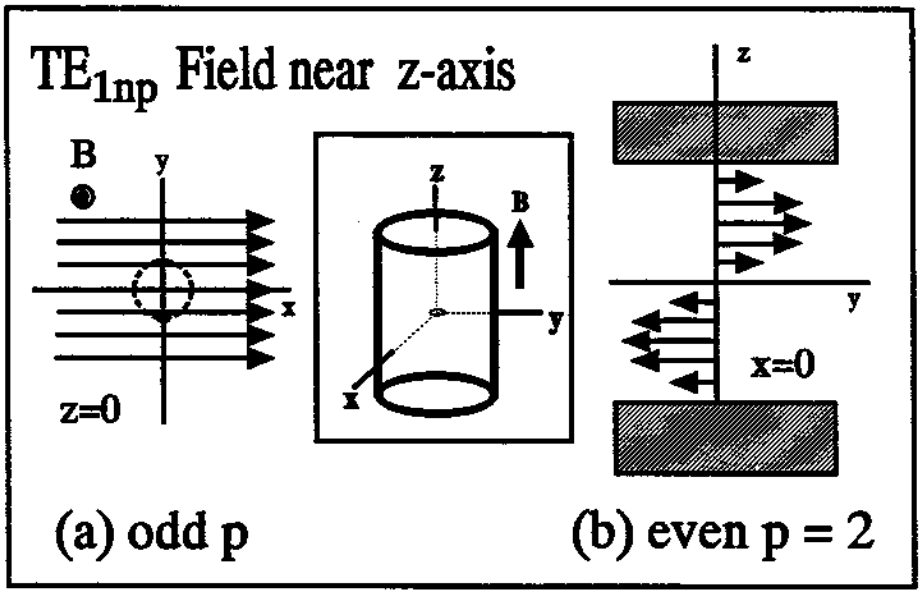

Figure 2.3: Representation of the transverse electric field for TE_{1np} modes: (a) in the midplane for odd p and (b) along the z-axis for even p.

components of the transverse electric field,

$$E_\perp = E_o \cos\left(\frac{\pi p z}{2z_0}\right) e^{-i\omega t}, \tag{2.2}$$

have a maximum in the midplane as illustrated in Fig. 2.3a. These odd p modes, with their electric field maxima near the trap center, couple strongly to electron cyclotron motion at the center of the trap. These modes are thus particularly suited for driving a centered cyclotron oscillator with an external microwave source. They provide efficient damping of electron cyclotron motion, as well, but also cause associated frequency shifts, as we shall see. For the related modes with p even,

the electric field vanishes in the midplane (Fig. 2.3b)

$$E_\perp = E_o \sin\left(\frac{\pi p z}{2 z_0}\right) e^{-i\omega t}. \tag{2.3}$$

The even p modes thus do not couple to the cyclotron motion of an electron at the center of the cavity. However, spatially displacing the electron from node to antinode provides a way to rapidly couple and uncouple the electron and cavity, turning the cyclotron damping from on to off. Moreover, the spatial gradients near the nodes are suited for sideband cooling thermal motions of the electron along the cavity axis.

Anywhere from 1 to more than 10^5 electrons can be localized within the cylindrical microwave cavity when the cavity walls are split to allow them to also serve as the electrodes of a Penning trap. A strong magnetic field confines the electrons radially, producing cyclotron oscillations. For precision experiments with the cyclotron motion, the magnetic field is required to be very uniform spatially and very stable in time [33]. This is provided by a specially designed superconducting solenoid system (Appendix A). In addition, an electrostatic restoring force along the z-axis (parallel to the magnetic field) keeps the electrons oscillating near the midplane of the cavity. Oscillations of the electrons along the magnetic field generate an observable current in a detection circuit connected to the trap electrodes.

Isolated electrons are confined in an ultra-high vacuum cavity attained by enclosing the trap in an evacuated envelope which is cryopumped because the envelope is kept at 4 K via thermal contact with a LHe bath. (A Long storage time limit, $\tau > 3.4$ months, of $\sim 10^3$ anti-protons in an open-access cylindrical trap used at CERN indicates that the vacuum in a cryopumped trap cavity can be better than 5×10^{-17} Torr. [36]) A field emission point is used to load electrons into the cavity. Electrons are stripped from the background gas by the $\sim$ 1keV electron beam from the field emission point entering along the trap axis through a 25 μm hole. (The field emission current strikes an electrode surface, removing adsorbed atoms into the cavity.) These secondary electrons are trapped as they dissipate energy via radiation into the cavity and via Joule heating of a detection

resistor. A good vacuum is restored after the field emission current is turned off. One electron has been continuously confined and studied in the cylindrical trap depicted in Fig. 2.1 for over two months before being ejected deliberately. (A 10-month confinement of one electron has been demonstrated in a hyperbolic trap. [31])

2.1 Sweeping the Cyclotron Frequency

In free space, the cyclotron oscillation of an electron decays due to synchrotron radiation. A microwave cavity formed by the metallic trap electrodes modifies the electromagnetic vacuum coupled to the electron oscillator, enhancing or suppressing radiation depending on the proximity of standing wave eigenfrequencies to the cyclotron oscillation frequency. Isolated electrons in a Penning trap cavity are well suited for radiative studies since the cyclotron frequency

$$2\pi\ \nu_c = \frac{eB}{mc} \tag{2.4}$$

is readily changed using the precisely controlled magnetic field. The coherent motions of parametrically-pumped electron oscillators studied here provide a new way to observe these cavity radiation modes by sweeping the magnetic field so that the electron oscillators are brought into resonance with the cavity modes. A magnetic field which is varying linearly in time is desirable.

Precise control of the cyclotron frequency is facilitated by the properties of a superconducting solenoid which provides the magnetic field. The current $J(t)$ in a superconducting solenoid of inductance L changes at a rate given by

$$\frac{dJ}{dt} = \frac{V}{L} \tag{2.5}$$

when a voltage source V is connected in series with the solenoid, according to Faraday's law. A model circuit is shown in Fig. 2.4 with a pure inductor representing a superconducting solenoid. Shunt resistor R has the combined resistance of a superconductive switch (present only when the switch is open) and a protection

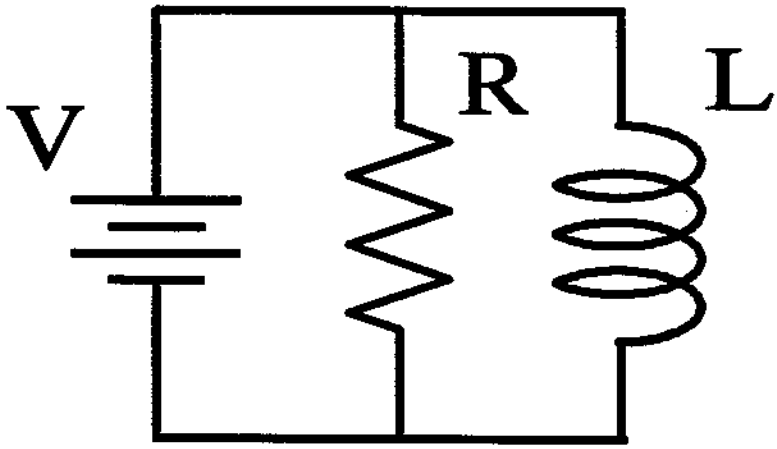

Figure 2.4: Model circuit for ramping the magnetic field in a superconducting solenoid.

resistor. The ideal voltage source must supply a current I(t) given by

$$I = \frac{V}{R} + J(t) \,, \tag{2.6}$$

where integration of Eq.(2.5) gives

$$J(t) = J(0) + \frac{V}{L}t \,. \tag{2.7}$$

Thus, electrons localized at the center of the solenoid experience a magnetic field varying linearly in time

$$B_z(t) = g\left(J(0) + \frac{V}{L}t\right) \tag{2.8}$$

where the coefficient g is calculable from the geometry and winding characteristics of the solenoid (Appendix A). Experimentally, the net current output I of the power supply is more readily monitored than the solenoid current J. The field $B_z(t)$ can be determined from the current supplied by the voltage source provided the "offset" current V/R drawn by resistor R is taken into account. It is convenient to introduce a time constant τ_o defined by

$$\frac{V}{R} = \frac{V}{L}\tau_o \tag{2.9}$$

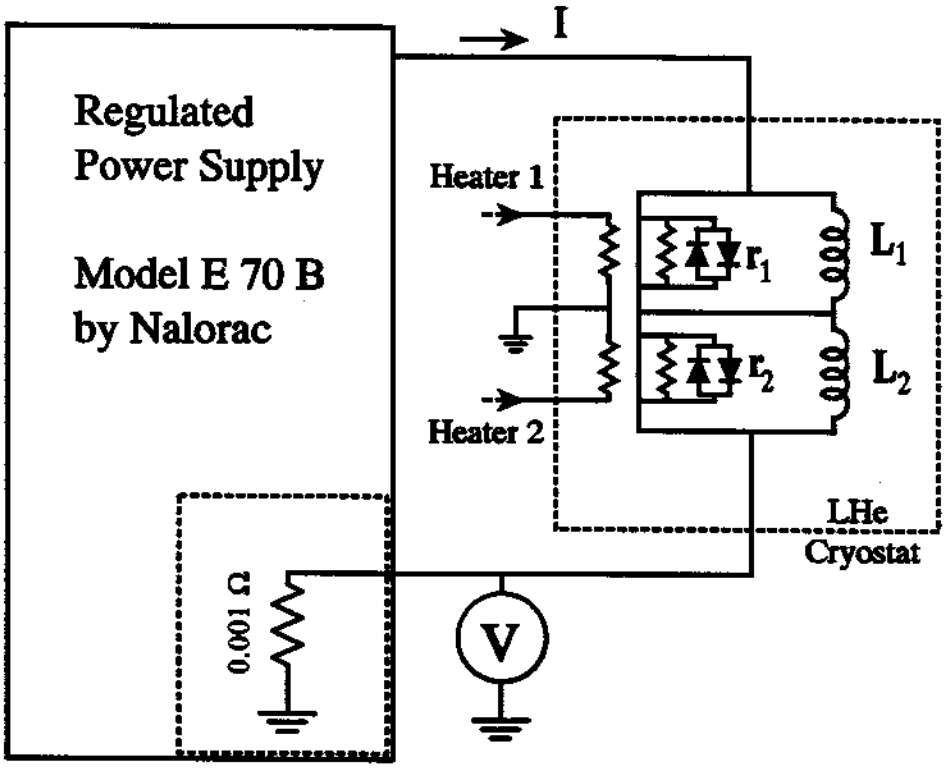

Figure 2.5: Simplified circuit representation of a Nalorac superconducting solenoid system, connected to a highly-regulated power supply.

so that the magnetic field is given by

$$B_z(t) = g\left[I(0) + \frac{V}{L}(t - \tau_o)\right], \tag{2.10}$$

in terms of measurable quantities. Alternatively, the cyclotron frequency is related to the current by

$$\nu_c(t) = \frac{\Delta\nu_c}{\Delta I}\left[I(0) + \frac{V}{L}(t - \tau_o)\right] \tag{2.11}$$

where the conversion factor $\Delta\nu_c/\Delta I$ is measured using a precision frequency synthesizer to drive a cyclotron resonance at a known current $I(0)$ with $V = 0$.

To attain high spatial homogeneity, some commercial superconductive magnets are constructed with circuits of more than one solenoid (Appendix A). Our

Parameter	Value	Unit
r_1	0.37 (7)	Ω
r_2	1.55 (2)	Ω
$L_1 + L_2 + 2M$	214 (2)	H
$\Delta\nu_c/\Delta I$	4.1854 (2)	GHz/A
τ_o	101 (1)	s
S	-4.1 (1)	—

Table 2.1: Measured properties of a traditional Nalorac superconductive magnet (JOB43).

Parameter	Value	Unit
$L_1 + L_2 + 2M$	207 (2)	H
$\Delta\nu_c/\Delta I$	4.1388 (2)	GHz/A
τ_o	102 (3)	s
S	-156(6)	—

Table 2.2: Measured properties of a new Nalorac superconductive magnet redesigned to be self-shielding (JOB51).

studies employed superconductive magnets (constructed by Nalorac Cryogenics Corp.) consisting of two solenoids to provide the high magnetic field. With appropriate generalization described below, the results for the simple solenoid also apply to a system with two solenoids. Fig. 2.5 shows a simplified circuit representation of a Nalorac superconductive magnet. To ramp the current in one solenoid, a small segment of the superconducting wire (a superconductive switch) can be turned normal (with a heater) if a matching current is provided by an external source. A highly-regulated power supply (model E70B by Nalorac) provides the matching current, monitors the charging voltage V across the system by remote sensing and maintains this voltage at a desired value. The net current output I of

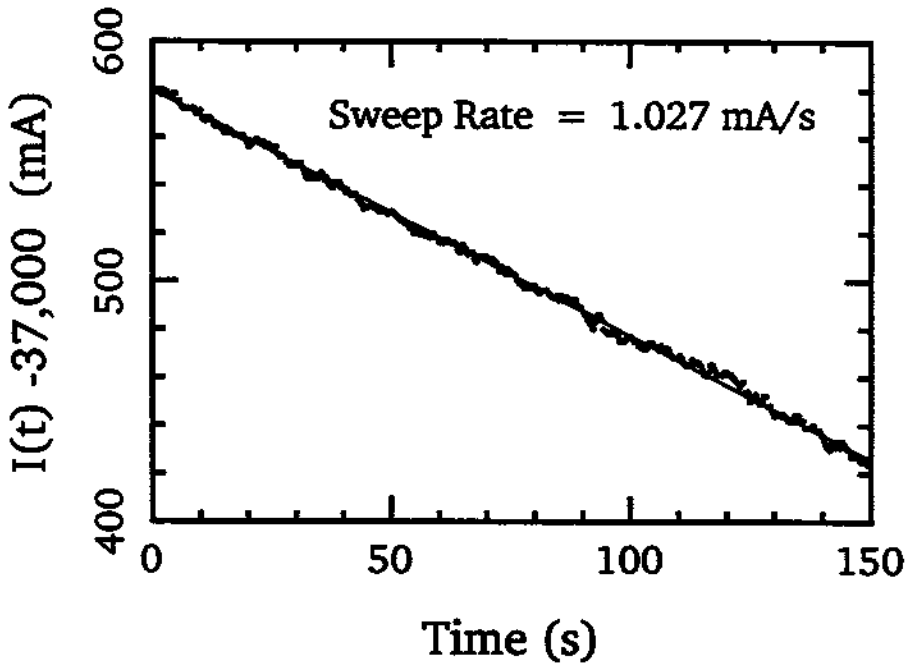

Figure 2.6: Measured current $I(t)$ versus time (dots) as the field in a superconducting solenoid system is ramped, and a linear fit (line).

the power supply is monitored on the return line using a precision resistor (0.001 Ω). The monitored current is digitized and stored in a computer to record the current continuously. As an example, Fig. 2.6 plots the return line current I versus time as the solenoid is discharged at a rate of $V/L = 1.0\text{mA/s}$. Measurement of the offset constant τ_o involves observation of a high-Q cavity mode for various charging rates V and will be discussed in Chapter 4. Measured characteristics for the superconductive magnets employed in our study are summarized in Table 2.1 and Table 2.2. Other characteristics calculated for these systems are tabulated in Appendix A.

In more detail, electrons localized near the center of a two-solenoid system (Fig. 2.5) experience

$$B_z(t) = g_1 J_1 + g_2 J_2 \quad , \tag{2.12}$$

which is a sum of contributions from current J_1 in solenoid L_1 with coefficient g_1

and from current J_2 in solenoid L_2 with coefficient g_2. Shortly after the heaters are activated, the currents J_1 and J_2 maintain a small difference proportional to the applied voltage V. When the currents in the two sections are equal (which occurs when $V = 0$), we have

$$B_z(t) = gJ_1 = gJ_2 \quad , \tag{2.13}$$

where $g = g_1 + g_2$. Relaxing within $\sim$ 3s after a voltage V is applied across the system, the currents J_1 and J_2 vary at the same constant rate V/L, where $L = L_1 + L_2 + 2M$ is the net inductance of the system with two solenoids (L_1 and L_2) having mutual inductance M. The offset current drawn by resistors r_1 and r_2 (Fig. 2.4b) is characterized by the time constant

$$\tau_o = \frac{1}{g}\left(\frac{g_1(L_1 + M)}{r_1} + \frac{g_2(L_2 + M)}{r_2}\right) \quad . \tag{2.14}$$

With these generalized definitions, Eq. (2.10) and Eq. (2.11) hold for two-solenoid systems. The case of a simple solenoid corresponds to $L_2 = M = g_2 = 0$.

2.2 Cylindrical Penning Trap

One electron experiments, in fact, require that the axial restoring force be nearly linear, as would be obtained from a high quality electrostatic quadrupole potential when appropriate voltages are applied to the trap electrodes. This results in harmonic oscillations of the trapped particle at well defined and precisely measurable frequencies, independent of small amplitude variations. For more trapped electrons, it is also convenient to use an electrostatic potential which can be precisely controlled and which is primarily an electrostatic quadrupole. In more detail, the desired electrostatic quadrupole potential can be written as

$$V = V_0 \frac{z^2 - \rho^2/2}{2d^2}[1 + C_2] \quad , \tag{2.15}$$

where V_0 is the the potential applied to the electrodes, d is an appropriate trap dimension (defined presently), and C_2 is a dimensionless constant which can be calculated from the electrode geometry. The axial dimension z is the distance from

the center of the trap along the magnetic field direction, ρ is the corresponding radial coordinate. A trapped particle of charge q and mass m oscillates harmonically in this potential, along the magnetic field direction, at axial frequency ω_z given by

$$\omega_z^2 = \frac{qV_0}{md^2}[1 + C_2] \ . \tag{2.16}$$

Typically the axial oscillation frequency is monitored precisely, with small shifts in this frequency used to derive information about the cyclotron and spin motions of the isolated electron.

Traditionally, such a potential was produced using Penning traps with metal electrodes painstakingly shaped along the hyperbolic contours which are the equipotentials of the desired electrostatic quadrupole. The microwave properties of a hyperbolic cavity, however, are not well understood. Our goal is to use the cylindrical trap cavity for controlling the radiation field. Hence, to approximate an ideal cylindrical cavity, the trap cavity in Fig. 2.1 was precisely constructed with small slits (0.013 cm) that incorporate choke flanges ($\lambda/4$ at 164 GHz). Although this cylindrical geometry is a much better way to understand and control the radiation field configurations in the trap cavity, it is a much less straightforward way to produce the high quality electrostatic quadrupole potential.

The trap cavity has its symmetry axis coincident with the vertical axis $\hat{z}$ parallel to a 6-T magnetic field from a superconducting solenoid. Small slits perpendicular to the magnetic field divide the oxygen-free high-conductivity copper cavity walls into two end-cap electrodes (at z_o above and below the trap center), a ring electrode (with radius ρ_o), and two compensation ring electrodes (with height Δz_c). A judicious choice of the ratio ρ_0/z_0 yields a crucial orthogonalization property [30]. Leading deviations which are unavoidably added to the desired electrostatic quadrupole potential in Eq. (2.15)

$$\begin{aligned} \Delta V \ = \ & \frac{1}{2}C_4V_0\frac{1}{d^4}\left(z^4 - 3z^2\rho^2 + \frac{3}{8}\rho^4\right) \\ & + \frac{1}{2}C_6V_0\frac{1}{d^6}\left(z^6 - \frac{15}{2}z^4\rho^2 + \frac{45}{8}z^2\rho^4 - \frac{5}{16}\rho^6\right) \end{aligned} \tag{2.17}$$

can be tuned (by adjusting potentials on the compensation electrodes [82]), with negligible change in the strength of the desired electrostatic quadrupole. More specifically, C_4 can be tuned over the range

$$10^{-5} < |C_4| < 10^{-1}, \tag{2.18}$$

while C_6 remains relatively constant at the large value [30]

$$C_6 \approx -10^{-1}. \tag{2.19}$$

Potentials on the trap electrodes are tuned to make the oscillation more harmonic, thus improving the observed signal-to-noise to the point that a resonant signal from just one trapped electron can be easily observed.

2.3 Observing A One Electron Oscillator

Once the potential is tuned, the motions of an isolated electron in a cylindrical trap are the same as in a hyperbolic trap. In the absence of damping, the exact equations of motions for one electron in a pure electrostatic quadrupole and uniform magnetic field are given by [10]

$$\ddot{z} + \omega_z^2 z = 0\,, \tag{2.20}$$

$$\ddot{\vec{\rho}} - \vec{\omega}_c \times \dot{\vec{\rho}} - \frac{1}{2}\omega_z^2 \vec{\rho} = 0\,, \tag{2.21}$$

where $\vec{\rho}(t) = x(t)\,\hat{x} + y(t)\,\hat{y}$ and a dot denotes the time derivative. The three familiar motions [10] include a cyclotron orbit around magnetic-field lines (at frequency $\omega_c'/2\pi < 170$ GHz), a harmonic axial oscillation along the magnetic field direction $\hat{z}$ (at frequency $\omega_z/2\pi = 63$ MHz) and a circular magnetron motion (at a much lower 12 kHz frequency) which is not important for the cavity electrodynamics. These harmonic motions are illustrated in Fig. 2.7. Cyclotron motion is damped because of its coupling to the radiation modes of a trap cavity. Axial oscillation is damped by a detection circuit connected to the electrodes. Fig. 2.8 shows a forced resonance of the damped axial motion for a single trapped electron, with

a linewidth which is less than 4 Hz. With this signal-to-noise ratio, a shift in the axial resonance frequency of 1 Hz out of 64 MHz is easily resolved, a resolution which is comparable with that obtained in hyperbolic traps [88,84,10]. Such high accuracy is needed in precision tests of fundamental physics, high-resolution mass spectroscopy, studies of single elementary particles and radiative studies. Specific examples which illustrate the sensitivity involved include the measurements of the anomalous magnetic moments $(g-2)$ of the electron and positron [88,84], the proton/electron mass ratio [85], observation of relativistic hysteresis and bistability

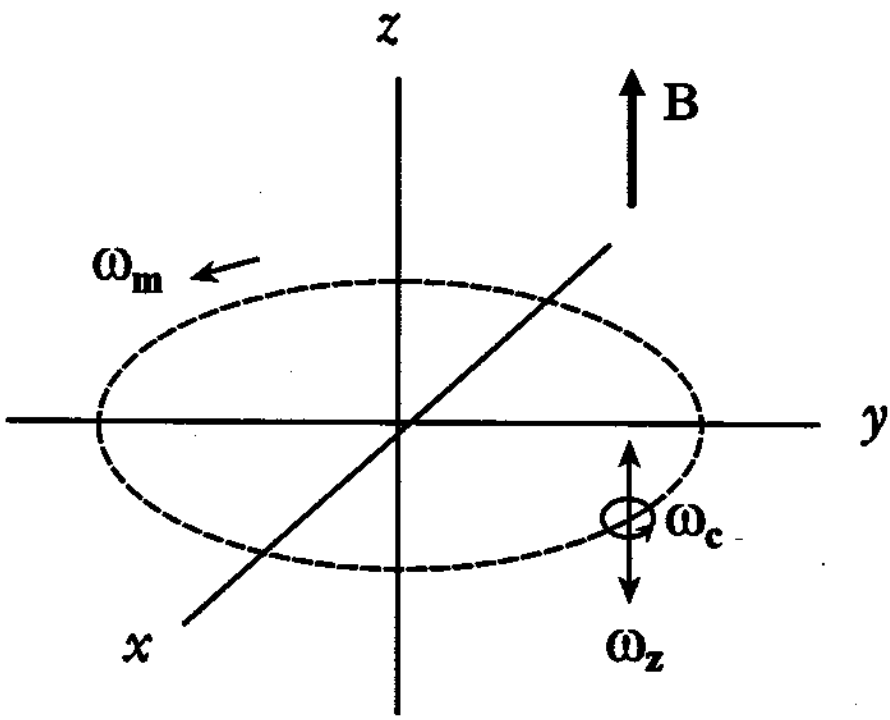

Figure 2.7: Motions of one electron confined in a Penning trap formed from a pure electrostatic quadrupole and a uniform magnetic field. "Guiding center" of fast cyclotron motion (at ω_c) oscillates along trap axis (at ω_z) and slowly drifts around the trap center (at ω_m).

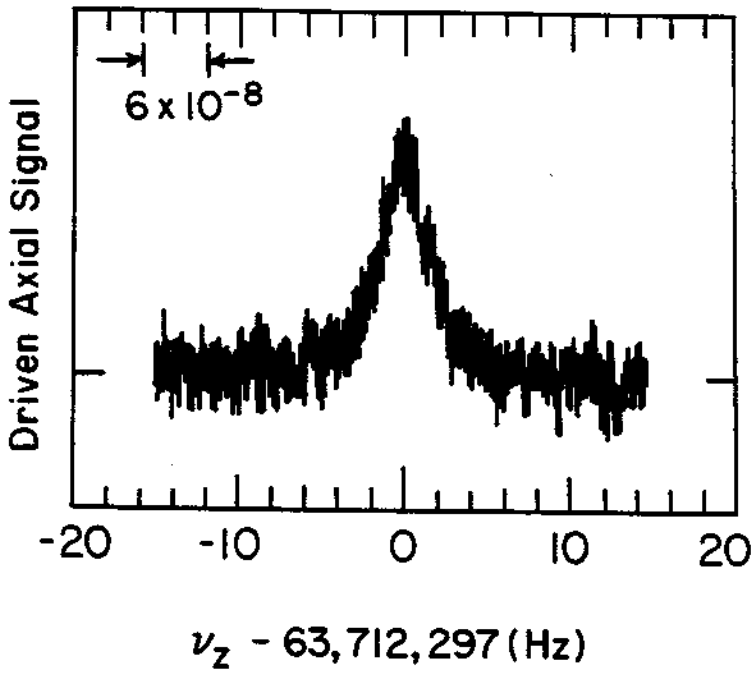

Figure 2.8: Driven axial resonance of one electron in a cylindrical Penning trap. [77]

of a single electron [31], and inhibition of spontaneous emission [32].

2.3.1 Minimizing Anharmonicity

Potentials $+\frac{1}{2}V_o$ on the flat endplates and $-\frac{1}{2}V_o$ on the center ring produce the electrostatic restoring force. Nonlinearity in restoring force causes amplitude-dependent frequency shifts and linewidth broadening in the resulting anharmonic particle oscillations. A potential V_c on the pair of compensation rings (Fig.2.9) must be adjusted [82] to minimize deviations from the electric quadrupole potential and thus make the axial restoring force as linear as possible. The height of these

electrodes

$$\Delta z_c/z_o = 0.2 \tag{2.22}$$

is sufficient to avoid an unacceptable sensitivity to the mechanical tolerances. A corresponding choice of radius [30]

$$\rho_o/z_o = 1.186 \tag{2.23}$$

was calculated to minimize the undesired frequency shifts which have been mentioned. We find it convenient to specify the size of the trap with a characteristic dimension $d = 0.355$ cm where d is defined by

$$d^2 = \frac{1}{2}\left({z_o}^2 + \frac{1}{2}{\rho_o}^2\right) \tag{2.24}$$

and $z_o = 0.3838(6)$ cm. Gaps between the electrodes (so different potentials can be applied to different electrodes) were made as small as practicable at 0.013 cm. The gaps were not expected to have major consequences [34].

For any axially symmetric trap, the electric potential near the trap center may be written as a series expansion given by

$$V(\mathbf{r}) = V_o\left(\frac{z^2 - \frac{1}{2}\rho^2}{2d^2}\right) + \frac{1}{2}V_o\sum_{\substack{n=0\\ \text{even}}}^{\infty} C_k\left(\frac{r}{d}\right)^k \mathrm{P}_k(\cos\theta) \tag{2.25}$$

where d is the characteristic length for this trap and the sum is over even n because of symmetry under reflections, $z \to -z$. The first term on the right is the desired electric quadrupole potential in cylindrical coordinates (ρ,z). The second term represents undesired additions in an imperfect trap, expanded in spherical coordinates (r,θ) and Legendre polynomials P_k. The expansion coefficients are linear in the compensation potential V_c

$$C_k = C_k^{(0)} + D_k\frac{V_c}{V_o} \tag{2.26}$$

with $C_k^{(0)}$ and D_k exactly calculable [30] using standard techniques [50] for perfectly aligned and cleaned conducting electrodes. The expansion converges rapidly for

particles near the center of the trap where $(r/d) \leq 10^{-2}$, so we only consider lowest order coefficients C_2 and C_4 (C_0 having no observable consequences for particles confined in the traps).

The compensation potential V_c is tuned to make $C_4 = 0$, thereby eliminating the leading deviation from a quadrupole potential. This occurs when $V_c/V_o = -C_4^{(0)}/D_4$ from Eq. (2.26). In practice, we tune V_c while monitoring the coherent

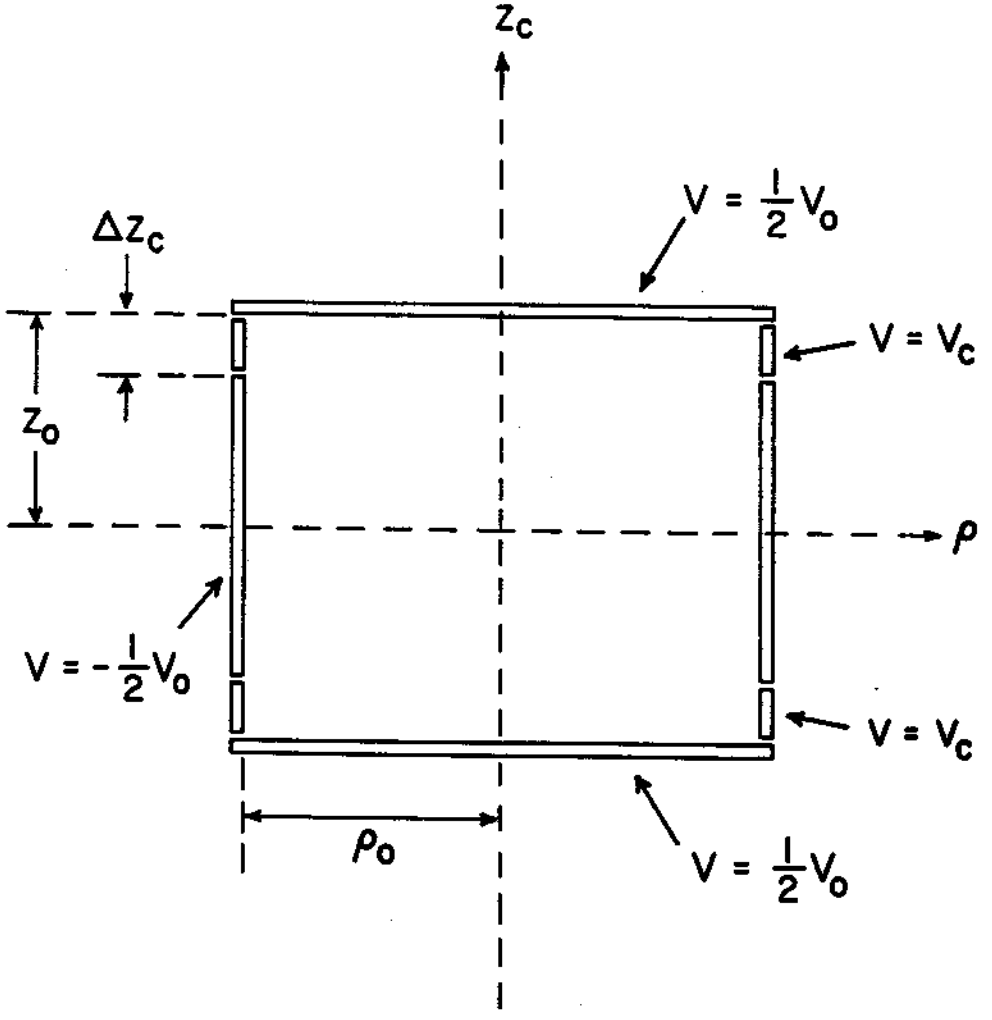

Figure 2.9: Simplified diagram of orthogonalized cylindrical trap. For the trap used, $\Delta z_c/z_o = 0.2$, and $\rho_o/z_o = 1.186$, $z_o = 0.3838(6)$ cm . The z-axis is aligned with a spatially uniform magnetic field.

response of a single trapped electron whose oscillatory axial motion along the magnetic field axis is being driven. For the trapping potential in this experiment ($V_o = 10.193\ V$) we must tune $V_c = 3.574\ V$ to get a symmetric resonance lineshape as shown in Fig. 2.8 and Fig. 2.10b. Thus, we get an experimental value of $V_c/V_o = -0.350(1)$ in good agreement with calculated value $V_c/V_o = -0.34(2)$, the uncertainty being due to the estimated mechanical tolerance of 8×10^{-4}cm in the dimensions and due to thermal contractions when the apparatus is submerged in liquid helium. The good agreement verifies the calculated value of $D_4 = -0.066(1)$. Detuning V_c to either side of this optimal value produces the characteristic skewed lineshape of an anharmonic oscillator. This is illustrated in Fig. 2.10a and Fig. 2.10c where V_c is +20mV and −20mV from the optimum, respectively. Since the compensation voltage must be tuned to within 1 mV of the optimal value to avoid an observable skewing of the resonance lineshape (e.g., Fig. 2.10), we use the calculated value of D_4 to conclude that we are able to tune $|C_4| < 10^{-5}$ in this trap.

2.3.2 Orthogonalized Electrodes

The adjustments to minimize deviations from the electrostatic quadrupole are generally attended by very inconvenient shifts in the resonant frequency of oscillation when the particles are driven along the magnetic field axis. In general, the axial resonance frequency ω_z will be shifted when V_c is changed since

$$\omega_z^2 = \frac{qV_o}{md^2}\left[1 + C_2^{(0)} + D_2\left(\frac{V_c}{V_o}\right)\right] \tag{2.27}$$

for the oscillation of a particle with charge q and mass m. Ideal electrode proportions would make $D_2 = 0$ so adjustments in the compensation potential leaves ω_z unchanged. A compensated Penning trap whose dimensions are selected to make $D_2 = 0$ is said to be "orthogonalized." Differentiating Eq. (2.27) and neglecting the small $C_2^{(0)} \sim 0.1$ we get

$$D_2 \approx \left(\frac{\partial \omega_z}{\partial V_c}\right) / \left(\frac{\partial \omega_z}{\partial V_o}\right) \ . \tag{2.28}$$

Using Eq.(2.28), we measure $D_2 \approx 2 \times 10^{-5}$ for this cylindrical trap, which is substantially smaller in magnitude than $D_2 \approx -5 \times 10^{-3}$ for the first generation hyperbolic traps used in so many precision experiments [88,31]. Fig. 2.10 illustrates how little ω_z shifts when a substantial adjustment of V_c to either side of the optimal tuning point, where the anharmonic distortions are clearly visible.

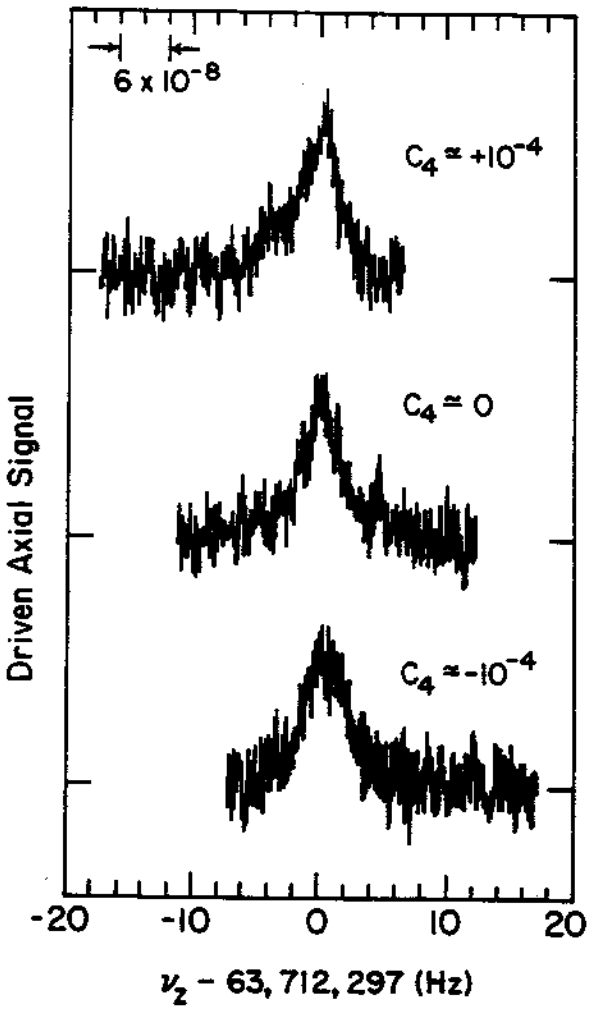

Figure 2.10: Driven axial resonance for one electron in the orthogonalized cylindrical trap. The middle curve (b) is the symmetric lineshape for a well-tuned trap ($C_4 \approx 0$). The characteristic lineshapes for an anharmonic oscillator are obtained when the potential V_c is adjusted so that $C_4 > 0$ in (a) and $C_4 < 0$ in (c). [77]

Comparable changes in the original hyperbolic traps would be accompanied by a frequency shift of about 500 linewidths.

A measure of the quality of an orthogonalized trap is how little the axial frequency ω_z changes for a given change in C_4. To quantify this a quality factor

$$\gamma_D \equiv D_2/D_4 \tag{2.29}$$

has been defined [28,30] with $\gamma_D = 0$ representing a perfectly orthogonalized trap. Using the measured value of D_2 and the calculated value of D_4 we obtained $\gamma_D \simeq 3\times10^{-4}$ which is a substantial improvement over $\gamma_D \simeq 0.56$ for the first generation hyperbolic traps.

2.3.3 Displacing the Axial Position

The potential within the trap when $\frac{1}{2}V_A$ and $-\frac{1}{2}V_A$ are applied to the upper and lower endcaps, with all the other electrodes grounded, is important for damping, driving and shifting the center of oscillation for the axial motion of trapped particles [29]. Near the center

$$V(\mathbf{r}) = \frac{1}{2}V_A \sum_{\substack{n=1\\ odd}}^{\infty} c_k \left(\frac{r}{d}\right)^k \mathrm{P}_k(\cos\theta) \tag{2.30}$$

with $c_1 = 0.784$ and $c_3 = 0.320$ calculated [30]. The product c_1c_3 can be easily measured [10] from the resulting frequency shift given by

$$\frac{\Delta\omega_z}{\omega_z} = -\frac{3}{4}\left(\frac{\mathrm{d}}{z_o}\right)^4 \frac{c_1c_3}{(1+C_2)^2}\left(\frac{V_A}{V_o}\right)^2. \tag{2.31}$$

We obtained $c_1c_3 = 0.26(1)$ which agrees with the calculated value. (These values for the cylindrical trap depicted in Fig. 2.1 provide neither advantages nor disadvantages relative to the hyperbolic traps.)

In chapter 4, rapid electronic control of electron-cavity interaction is demonstrated by shifting the axial positions of trapped electrons in a standing wave of the cavity. With the potential of Eq. (2.30), electrons near the trap center are shifted along the z-axis by

$$z_e = \frac{1}{2}\frac{c_1}{1+C_2}\left(\frac{V_A}{V_o}\right)d\,. \tag{2.32}$$

For the trap of Fig. 2.1 ($C_2 = 0.128$ and $d = 3550\mu$m), a trapping potential of $V_o = 10.2$ Volts yields

$$z_e = \left(121\frac{\mu\text{m}}{V}\right) V_A \ . \tag{2.33}$$

Thus, applying $V_A = 4.55$ Volts should shift electrons from anti-node to node (or vice-versa) of a standing wave with 550 μm quarter-wavelength along the z-axis (such as TE_{027}).

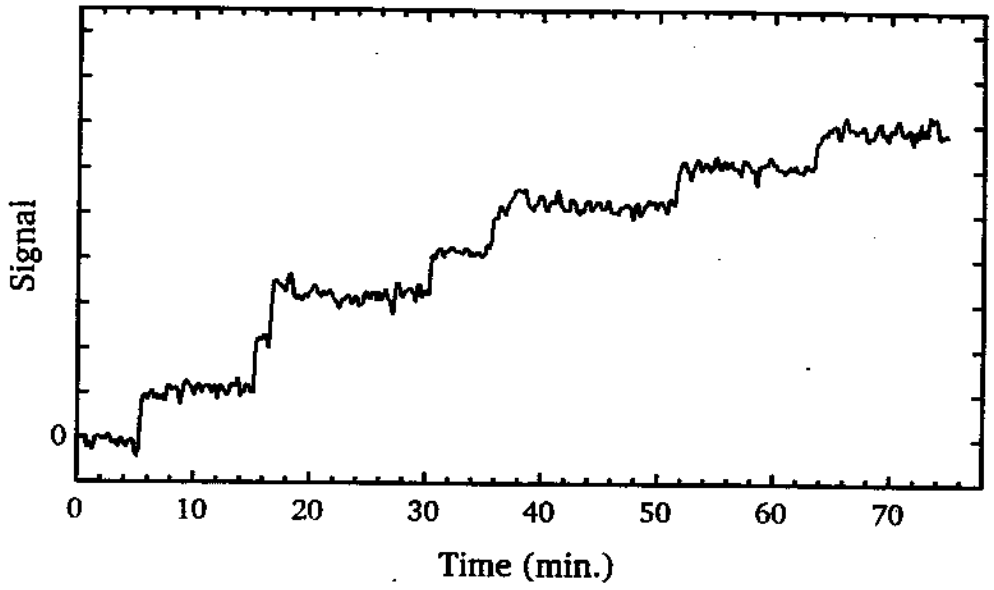

Figure 2.11: Detection of 7 electron oscillators loaded into a cylindrical Penning trap cavity sequentially.

2.4 Counting Electron Oscillators

Electrons confined in the trap cavity can be counted in non-destructive ways. This allows collective behavior to be studied in a wide range of electron numbers, ranging from small dynamical systems with as few as two electrons to "microplasmas" with as many as 10^5 electrons. Fig. 2.11 shows a signal changing in discrete increments as 7 electrons are loaded in sequence into the cavity. The signal is derived from the induced current through a resistor when the electrons are forced at a frequency ω_f fixed at a large detuning below the resonance frequency ω_z. Forced

axial CM motion of N electrons (each of mass m and charge q) satisfies

$$m\left[\frac{d^2}{dt^2} + N\gamma_z\frac{d}{dt} + (\omega_z)^2\right] z(t) = \kappa\frac{qV_d}{d}\sin(\omega_f t + \phi) \tag{2.34}$$

where γ_z is the damping for one electron and V_d is the drive strength. A commercial lock-in amplifier is used for phase-sensitive detection of the driven response, with the in-phase component of the signal given by

$$S_I = \alpha V_d \frac{(N\gamma_z/2)^2}{(N\gamma_z/2)^2 + \Delta\omega^2} \tag{2.35}$$

and the quadrature component of the signal given by

$$S_Q = \alpha V_d \frac{(N\gamma_z/2)\ \Delta\omega}{(N\gamma_z/2)^2 + \Delta\omega^2} \tag{2.36}$$

where $\Delta\omega = \omega_f - \omega_z$. For large detuning ($|\Delta\omega| >> N\gamma_z$), the quadrature component is proportional to the number of particles and thus generates the step structure shown in Fig. 2.11 as a low field emission current slowly loads electrons into the cavity. The number of particles in a large system is more readily determined from the linewidth of the forced resonance. Fig. 2.12 shows the in-phase (a) and quadrature (b) signals as the drive frequency is swept through resonance. Comparison of the linewidth from either component with that of a single electron (Fig. 2.8) indicates that $N = 10^3$. For systems so large that the CM motion couples strongly to the detection circuit, the number of particles can be determined from the Fourier spectrum of the noise-driven coupled system, as discussed in Appendix B.

2.5 Detection and Damping of Axial Motion

An electron near the center of the cavity executes simple harmonic motion along the magnetic field. Axial oscillation plays an important role in many experiments because a shift in its resonance frequency can be used to observe the states of the other motions. To detect the axial motion, an inductor is connected to one endcap and AC grounded with the remaining electrodes. The voltage across the inductor

is monitored. The resonance frequency of the resulting tank circuit (formed by trap electrodes and the coil) is typically tuned to the oscillation frequency of the axial motion. Under this condition, the capacitive reactance of the electrodes is cancelled by the inductive reactance of the coil and the tuned circuit is effectively a resistor R. The current induced through the resistor R by axial motion produces

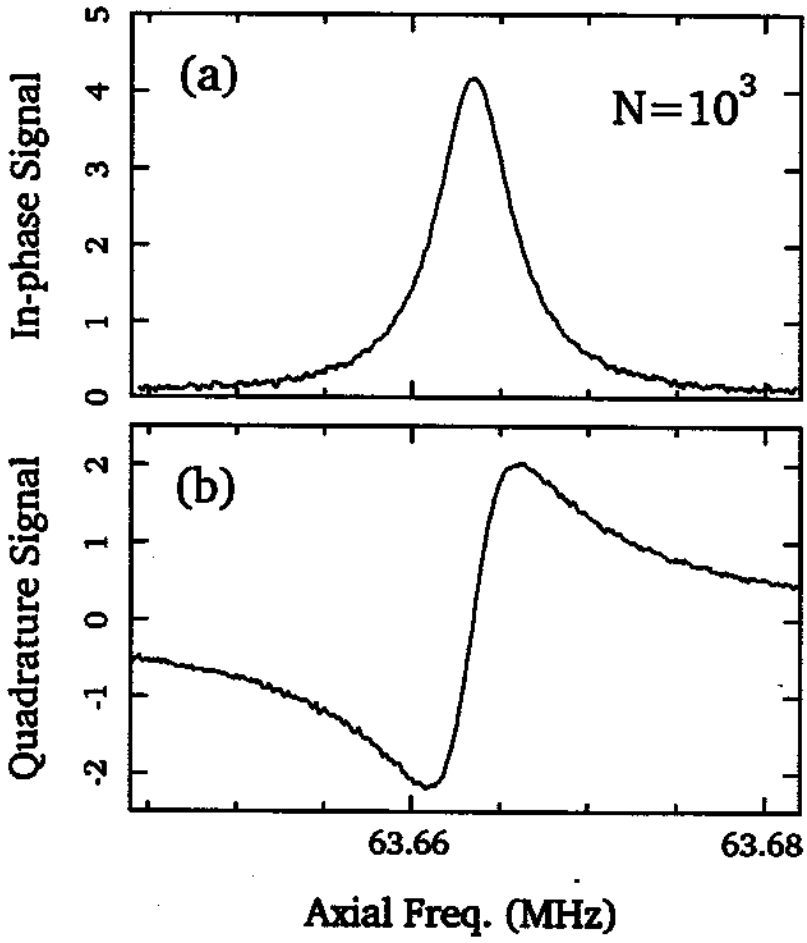

Figure 2.12: Driven resonance for an electron cloud observed using phase-sensitve detection, with in-phase component in (a) and quadrature component in (b).

a voltage given by [73,29]

$$V(t) = -\left[\frac{\kappa q}{2z_o}\right] \dot{z}(t)\ R\ . \tag{2.37}$$

The induced RF current ($V/R \propto \dot{z}$) dissipates energy in the resistor and thus damps the axial motion as indicated earlier in Eq. (2.34). A resonant force is applied using RF fields to excite the damped oscillator. The observed voltage across the resistor is monitored with a dual-gate, GaAs MOSFET pre-amplifier which is submerged in LHe to minimize thermal noise. After further amplification, various electronics are used to extract amplitude and phase information about the electron motions from the processed signal.

2.5.1 Interaction with a Tuned Circuit

Interaction of the electron axial oscillator with an LCr circuit allows the axial oscillation to be observed and the damping rate to be precisely controlled. Axial oscillation $z(t)$ induces a current in an LCr circuit formed by a helical resonator (with inductance L) connected across an endcap and ring electrodes of the trap (with effective capacitance C). The oscillating current $\dot{Q}(t)$ in the tuned circuit, in turn, produces an RF electric field which acts back on the electron. This electromechanical system is represented in Fig. 2.13 and the coupling between the two oscillators is described by the interaction potential

$$V_{int} = -\left[\frac{\kappa q}{2z_o C}\right]\ z(t)\ Q(t). \tag{2.38}$$

The dimensionless coupling constant κ has value $\kappa = 1$ for a capacitor with infinite parallel plates (separated by $2z_o$). (For our actual trap electrodes $\kappa = c_1 = 0.784$ has been calculated [30].) The equations of motion are

$$L\left[\frac{d^2}{dt^2} + \Gamma_M \frac{d}{dt} + (\omega_M)^2\right] Q(t) + \left[\frac{\kappa q}{2z_o C}\right] z(t) = 0 \tag{2.39}$$

$$m\left[\frac{d^2}{dt^2} + (\omega_z)^2\right] z(t) + \left[\frac{\kappa q}{2z_o C}\right] Q(t) = F(t) \tag{2.40}$$

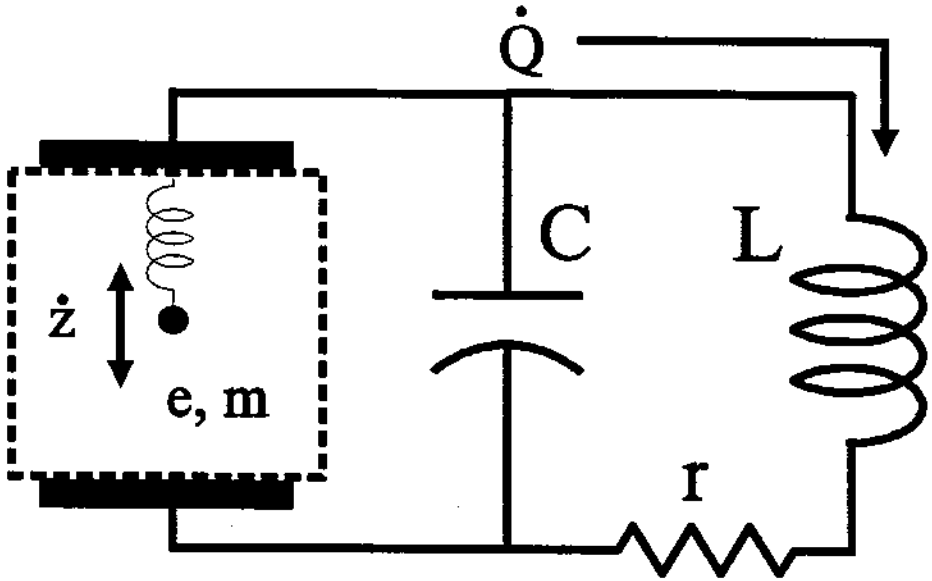

Figure 2.13: Electromechanical representation of a harmonically-bound electron coupled to a tuned circuit.

The resonance frequencies of the tuned circuit and electron oscillator are ω_M and ω_z, respectively, when the interaction is turned off. The right hand side of Eq.(2.39) is set to zero since we are neglecting the Johnson noise (Appendix B) due to the resistor. This coupled system also serves as a simple model for electron-cavity interaction (Chapter 4).

The tuned circuit, as indicated by Eq. (2.39), is a damped, harmonic oscillator which is driven by the electron oscillation. The oscillating current $\dot{Q}(t)$ in the helical resonator damps out at a rate $\Gamma_M = r/L$. Observed signal is derived from the voltage across the inductor

$$V_L = L\ddot{Q}(t) \; . \tag{2.41}$$

When $\omega_z = \omega_M$, this voltage is given by Eq. (2.37) in terms of the the effective

parallel resistance

$$R = \frac{L}{rC}. \tag{2.42}$$

We will often find it convenient to use this simplification.

2.5.2 Signal Amplification

The signal generated by driven electrons is generally very weak. For example, the response from a single electron dissipates only 10^{-20} Watt of power in the tuned circuit. To provide enough power to drive the low input impedance of the

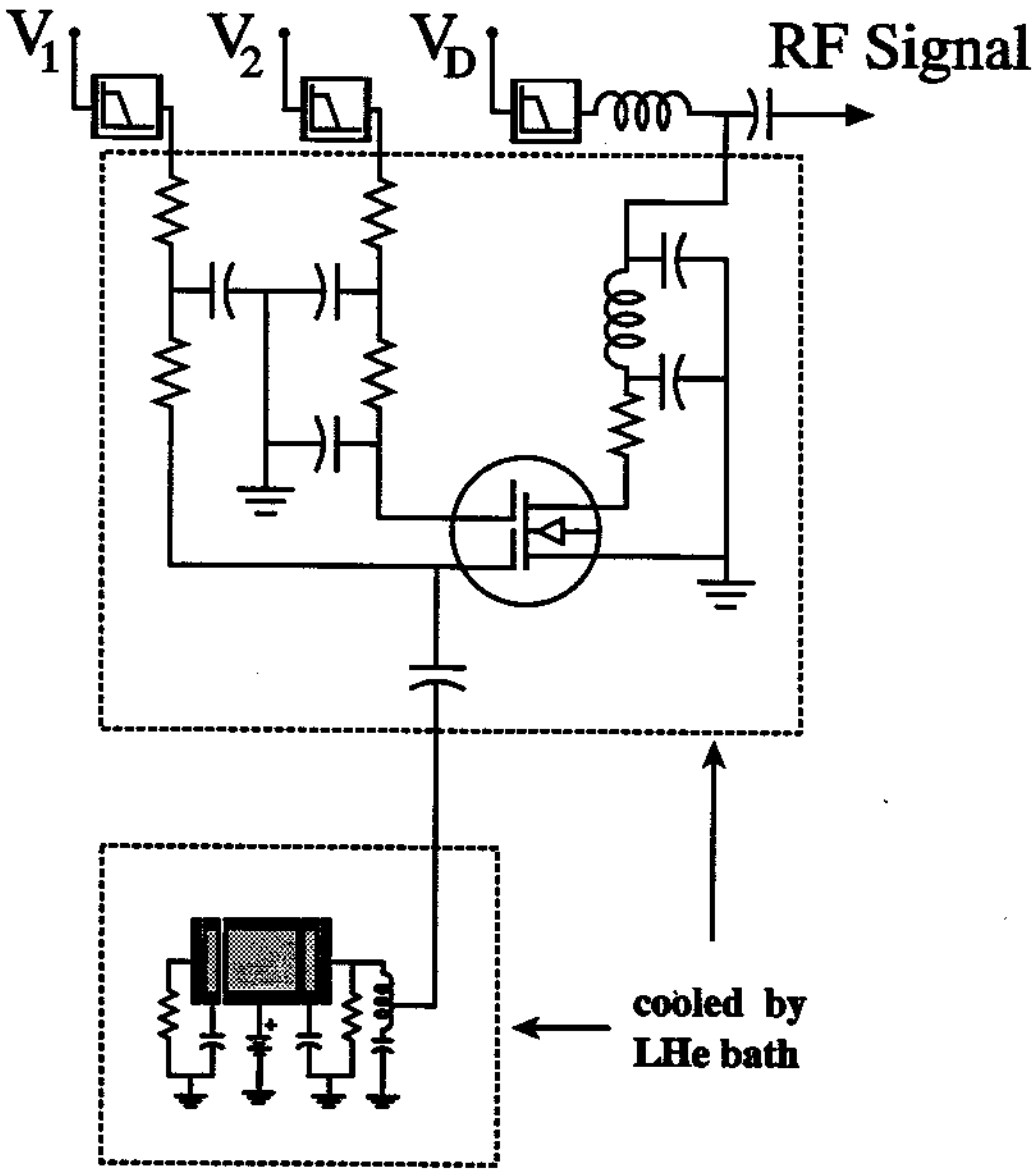

Figure 2.14: A dualgate MOSFET pre-amplifier monitors induced voltage across tuned circuit.

amplifier chain, a dualgate gallium arsenide MOSFET circuit (Fig. 2.14) serves as a pre-amplifier for the weak induced voltage across the helical resonator. This FET pre-amplifier is cooled by thermal contact with a LHe bath to reduce thermal noise. The size of signal and time scale of interest span many orders of magnitude in our study of collective behavior, requiring some important modifications (Fig. 2.15) which have been made to optimize an otherwise traditional electrical set-up [18,93,94,87]. Wideband amplifiers increase the signal from the FET pre-amplifier by a gain of 34 dB. This signal is mixed down to an intermediate frequency (5 MHz), passed through a crystal filter (6 kHz bandpass centered at 5 MHz) and amplified further with a gain of 40 dB. The amplified signal at this frequency can be further processed in various ways using, for example, a storage oscilloscope, a lock-in amplifier and square-law circuits. A splitter sends the signal simultaneously to these devices.

2.5.3 Phase-sensitive Detection

A lock-in amplifier converts the IF signal (5 MHz) into a DC output which is a function of the relative phase between the local oscillator and the forced response [10]

$$S_D = V_d \frac{(\Gamma_z/2)^2 \cos\phi + (\Gamma_z/2)\,\delta\omega_d \sin\phi}{(\delta\omega_d)^2 + (\Gamma_z/2)^2} \quad . \tag{2.43}$$

The relative phase ϕ is varied with the phase-shifter in the lock-in amplifier. This phase-sensitive signal S_D (output A in Fig. 2.15) also depends on the damping rate $\Gamma_z = N\gamma_z$, on the drive strength V_d and on the detuning $\delta\omega_d$ between the drive frequency and the electron oscillator frequency. Fig. 2.12a shows the absorptive signal ($\phi = 0$), and Fig. 2.12b shows the dispersive signal ($\phi = 90°$) for $N = 10^3$ electrons, obtained by sweeping the drive frequency. The full width at half maximum of the Lorentzian lineshape gives the axial damping rate Γ_z, which is used to determine the number of electrons, as already shown.

As we have mentioned, the resonant response to parametric excitation can have one of two steady-state phases which differ by 180° . Since $S_D \rightarrow -S_D$ when

$\phi \rightarrow \phi \pm \pi$, a transition between the phase-bistable states of a parametrically-driven electron can be detected. However, the shortest integration time constant available in our commercial lock-in amplifiers is 10 ms. Hence, to observe the fastest transitions which occur in parametrically-pumped electrons, we bypass this lock-in amplifier, mix the signal with a local oscillator to produce "baseband"

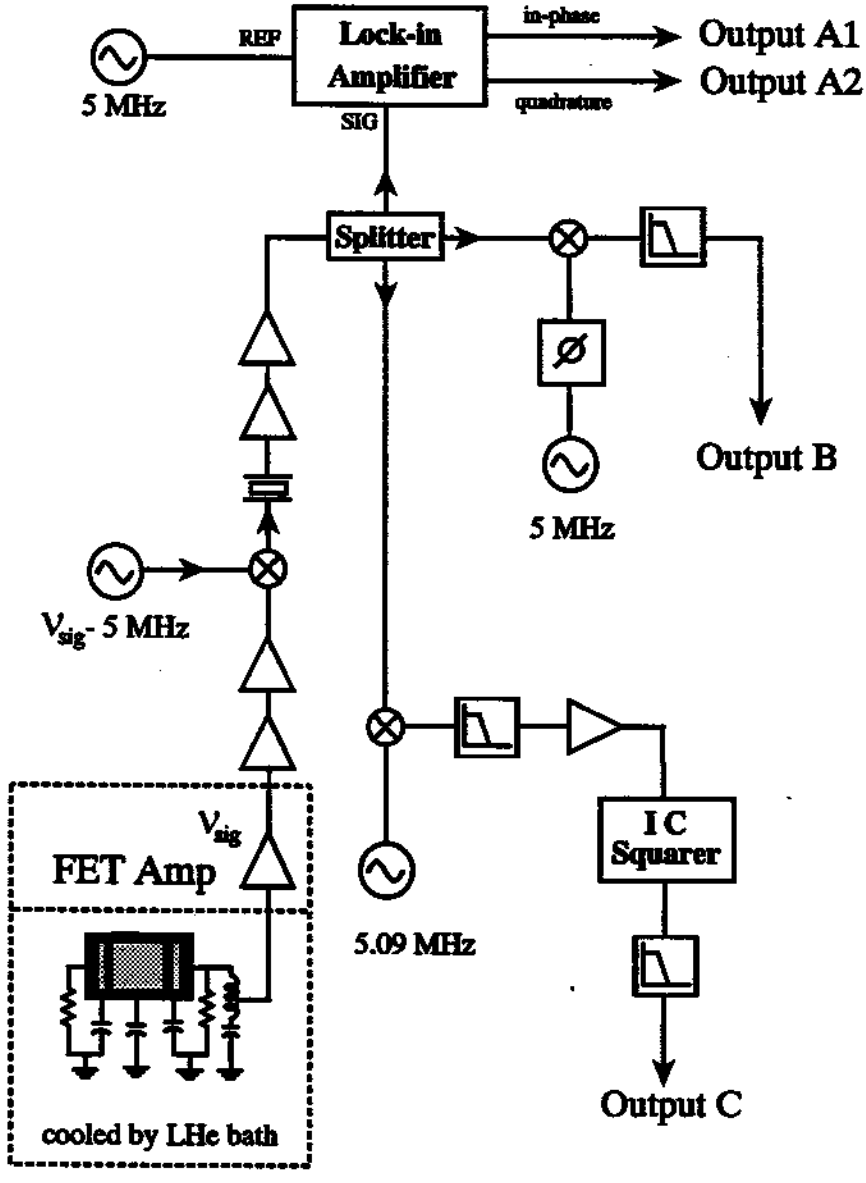

Figure 2.15: Schematic diagram of electrical set-up for processing observed signal.

output and use a storage scope (output B in Fig. 2.15).

2.5.4 Center-of-mass Energy Detection

In some experiments, the amplitude or energy in the axial CM motion is of interest. To measure energy in the CM motion, the response signal is squared and a low-pass filter removes the AC component to obtain a baseband signal which is proportional to the squared amplitude (or energy) of the CM motion (output C in Fig. 2.15). We use a multiplier chip (Analog Devices AD532K) designed for precision instruments to implement

$$V_{out} = \frac{(V_{in})^2}{10} , \tag{2.44}$$

where V_{in} and V_{out} are given in Volts. The accuracy is better than 10% for output in the range of 9 mV to 14V and is better than 5% for output in the range of 25 mV to 10 V. Traditionally, passive diode square-law circuits have been used for this purpose but with narrower operating voltage range (typically 10 times narrower). Unlike the typically weak stochastic signal which these passive diode circuits have been constructed to observe, the coherent response of parametrically-pumped electrons can vary by many orders of magnitude. The better performance of the IC squarer is very useful in establishing the lineshapes of cavity mode resonances which are clearly observed using the coherent motions of parametrically-pumped electron oscillators.

2.6 Forced Excitation

To excite the axial motion which is damped by the tuned circuit, a sinusoidal force $F(t) = F_o \sin(\omega t + \phi)$ can be applied using precision frequency synthesizers. If the rate of energy exchange between the two coupled oscillators is much slower than the rate of resistive dissipation in the tuned circuit (weak-coupling regime), then the differential equation for the axial motion, Eq.(2.40), can be simplified

into one describing a forced, damped, harmonic oscillator

$$m\left[\frac{d^2}{dt^2} + \gamma_z\frac{d}{dt} + (\tilde{\omega}_z)^2\right] z(t) = F_o \sin(\omega t + \phi) \ , \tag{2.45}$$

with a damping rate γ_z. The resonance frequency ω_z of the oscillator is shifted ($\omega_z \longrightarrow \tilde{\omega}_z$) due to interaction with the tuned circuit. The shift $\Delta\omega = \tilde{\omega}_z - \omega_z$ does not exceed one fourth of the maximum linewidth, but must be taken into account to be within range of parametric resonance. Helical resonators using silver-coated or superconducting wire have high quality factor at LHe temperature ($Q > 600$), allowing a further simplification of the damping and frequency shift due to the tuned circuit

$$\gamma_z = \gamma_{zo}\frac{1}{1+\delta^2} \ , \tag{2.46}$$

$$\tilde{\omega}_z - \omega_z = \frac{1}{2}\gamma_{zo}\frac{\delta}{1+\delta^2} \ . \tag{2.47}$$

These forms are illustrated in Fig. 1.1. The detuning δ is defined by $\delta = 2(\omega_z - \omega_M)/\Gamma_M$. The maximum damping rate, given by [18,93]

$$\gamma_{zo} = \left[\frac{\kappa q}{2z_o}\right]\frac{R}{m}, \tag{2.48}$$

with effective parallel resistance $R = L/rC$, is obtained when electron and helical resonator are tuned to the same frequency ($\delta = 0$). Damping can be reduced by adjusting the detuning δ. Control of resistive damping is important for studying parametrically-pumped electron oscillators. Interestingly enough, the electromechanical system of Fig. 2.13 also provides a model for understanding electron-cavity coupling. The frequency shift, which is maximum at $\delta = \pm 1$, has serious implications for some precision experiments (Sec. 4.4).

The description given above for one electron also applies to a system of N electrons provided $z(t) \longrightarrow Z(t)$ to represent the axial center-of-mass (CM) coordinate; $m \longrightarrow Nm$, the total mass; and $q \longrightarrow Nq$, the total charge of the cloud. The damping rate for the axial CM motion is proportional to N

$$\Gamma_z = N\gamma_z \tag{2.49}$$

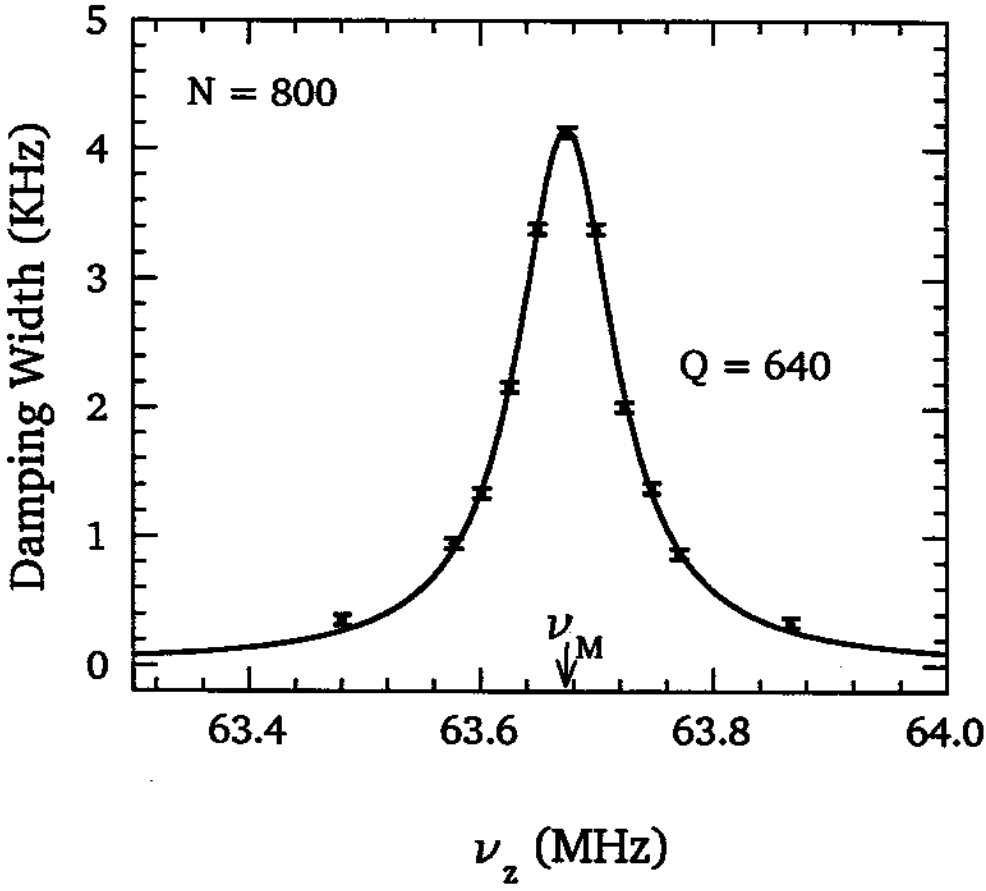

Figure 2.16: Lorentzian form fits well to measured damping width of driven resonance versus oscillation frequency ν_z near the resonance frequency ν_M of tuned circuit.

where γ_z is $(30\ \text{ms})^{-1}$ at maximum for one electron. The damping width can be measured from the FWHM width of the Lorentzian lineshape (Fig. 2.12) of the in-phase signal from a phase-sensitive detector, as already mentioned. Fig. 2.16 plots the measured resonance linewidth as a function of detuning from the tuned circuit for $N = 800$ electrons. Variation of observed linewidths with detuning δ fits well to a Lorentzian lineshape, as expected from Eq. (2.46). Quality factor of the helical

resonator measured from Fig. 2.16 is in good agreement with that obtained from Johnson-noise-driven resonance of the tuned circuit (Appendix B). As already shown, Eq. (2.49) allows N to be determined by comparison with the driven resonance linewidth for one electron γ_z. For large number of electrons ($N \gg 10^3$), the axial frequency must be sufficiently detuned from the LCr frequency in order for Eq. (2.49) and for weak-coupling approximations to be valid. When coupling between the tuned circuit and a very large number of electrons is too strong, the noise-driven Fourier spectrum of the resonantly coupled system can be used to measure N (discussed in Appendix B).

Forced excitation, Eq. (2.45), can be accomplished by applying a single RF electric field near to resonance with the electron axial frequency. This method is not used in practice because a direct, resonant drive will saturate the high-gain chain of amplifiers used to observe the small signal of driven electrons ($V_L \sim 20\text{nV}$ for one electron). To avoid stray coupling (such as capacitive coupling) between the drive and detection electrodes with a resonant RF field, two RF fields of lower frequencies are used to drive the electrons. We briefly summarize the essential features since the mechanism has been treated in detail elsewhere [10]. The spring constant of the axial oscillator is modulated at a fixed frequency ω_1 which is much lower than the resonant frequency $\tilde{\omega}_z$ (shifted by tuned circuit). Another frequency synthesizer drives the electron at a frequency ω_d which can be varied, so that

$$F_o \sin(\omega_d t + \phi) = m\left[\frac{d^2}{dt^2} + \Gamma_z \frac{d}{dt} + (\tilde{\omega}_z)^2 (1 + \epsilon \cos(\omega_1 t))\right] z(t) \quad , \qquad (2.50)$$

where $\epsilon \ll 1$ is the ratio of the modulation amplitude to the static trapping potential. An observable response is obtained by sweeping the drive frequency ω_d so that

$$\omega_d = (\tilde{\omega}_z - \omega_1) + \delta\omega_d \qquad (2.51)$$

where $\delta\omega_d$ is a drive detuning from resonance. The effective force produced in this manner is the same as the direct drive in Eq.(2.45), with the exception that the effective force is smaller in amplitude by a factor $\beta/2$. The "modulation index" β

is given by [10]

$$\beta = \frac{\epsilon}{2}\frac{\tilde{\omega}_z}{\omega_1} \ . \tag{2.52}$$

2.7 Parametric Excitation

Throughout this study, the cooperative phenomena of interest are observed when trapped electrons are pumped parametrically at a frequency $\omega_d \approx 2\omega_z$ which is approximately twice the axial oscillation frequency. To accomplish this, the otherwise static potential in Eq. (2.15) is modulated using a precision frequency synthesizer. The resulting axial restoring force has a spring "constant" with a small periodic component, i.e.,

$$m\omega_z^2 \longrightarrow m\omega_z^2\left[1 + h\cos(\omega_d t)\right] . \tag{2.53}$$

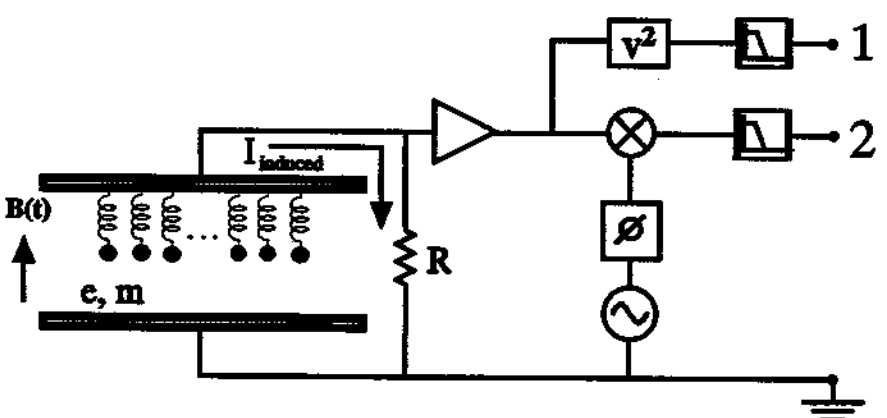

Figure 2.17: Simplified diagram showing detection electronics used in observing parametrically-pumped electron oscillators (modeled as massive, charged balls attached to springs).

Both the strength of the parametric drive, h, and its frequency ω_d are varied as part of these studies. A simplified model which gives the important features of the system under study is presented in Fig. 2.17. A trapped electron is modeled as a ball of charge q and mass m suspended from an axial spring whose spring constant has just been discussed. The trap electrodes are involved in the detection of the axial motion of the center of mass of the trapped electrons in a way that can be represented by the parallel plates in the figure. We observe the current induced through the resistor R connected across the parallel plates. (For simplicity, the axial oscillation frequency is tuned to the resonant frequency of the LCr circuit so that it can be effectively replaced by a resistor R.) Power dissipated in the resistor is responsible for the axial damping which has been mentioned. The voltage across resistor R (proportional to the velocity of the CM motion) is amplified and electronically processed to give the CM energy (output 1 in Fig. 2.17) and the phase of the CM motion (output 2 in Fig. 2.17) relative to the parametric pump. Because the pump is at twice the response frequency, any coherent (steady-state) response of the electron cloud (not previously observed) must have either of bistable phases that differ by 180°. Transitions between these phase-bistable states can be observed via output 2 in Fig. 2.17. This simplified picture omits several features that are important. First, the perpendicular motions of the electrons are important, with the fast cyclotron motions of the electrons about the strong magnetic field radiating into the surrounding microwave cavity to cool the system. Inter-particle Coulomb repulsion couples the oscillators and is crucial for collective motions. Further, energy exchange occurs between the axial and perpendicular motions.

Instead of applying an RF potential (at $\omega_d \approx 2\tilde{\omega}_z$) between the ring electrode and both endcaps to produce the desired modulation

$$V_o \longrightarrow V(t) = V_o\,[1 + h\ cos(\omega_d t)]\,, \tag{2.54}$$

it is experimentally convenient to apply the RF drive between one endcap and the ring electrode. The resulting RF field at the trap center has a symmetric and

anti-symmetric component. Only the symmetric field contributes significantly to parametric excitation, with effective modulation strength which is smaller by 6 dB. The anti-symmetric component, in principle [59], can produce parametric resonance if the trapping potential has a cubic anharmonicity of the form

$$\Delta V = \frac{1}{2} c_3 \left(\frac{Z}{z_o}\right)^3 V_A \tag{2.55}$$

where $V_A < 10^{-4} V_o$ is a very small imbalance in the applied trapping potential. The relative modulation strength of the anti-symmetric component compared to the symmetric component is given by

$$\frac{h_{anti}}{h_{sym}} = \frac{1}{2} \frac{c_1 c_3}{(1+C_2)^2} \left(\frac{d}{z_o}\right)^4 \left(\frac{V_A}{V_o}\right). \tag{2.56}$$

The coefficients $c_1 c_3$, and C_2 have been measured (mentioned earlier). In practice, this ratio is negligibly small ($\sim 10^{-5}$) and hence only the symmetric modulation of the trapping potential contributes to parametric resonance.

2.8 Summary

Electrons isolated in a cylindrical cavity provide a new system for radiative experiments with standing wave modes having well-known field configurations. Anywhere from one to over 10^5 electron oscillators can be confined in a cylindrical Penning trap which is constructed to be the best approximation to an ideal microwave cavity. The electrons can be displaced along trap axis to probe the standing wave patterns. The cyclotron frequency is readily varied to selectively couple with a cavity mode of interest. A cylindrical Penning trap thus allows precise control of electron-cavity interaction (Chapter 4). On the other hand, it requires a large correction potential V_c to minimize deviations from a pure electric quadrupole (which insures harmonic axial oscillation at well-defined frequency needed for precise experiments with one electron). Traditionally, necessary corrections are reduced by employing trap electrodes shaped along hyperbolic contours, but residual anharmonicity is unavoidable due to imperfections and misalignments

as well as holes and slits. Analysis [28,29] of the electrostatic properties of hyperbolic traps suggested that the need for hyperbolic electrodes may not be as strong as had been assumed. Fortunately, the electrostatic properties for cylindrical traps can be calculated analytically, greatly facilitating the design of an "orthogonalized" set of cylindrical electrodes [30] which allows large adjustments to be made to restore a high quality electric quadrupole. Cylindrical electrodes can be machined to higher accuracy in less time. We have now demonstrated that the simpler, cylindrical traps can be utilized even for the precise measurements with one electron (already mentioned), with the added advantages of a well-characterized microwave cavity. [77] A single electron has been observed with a signal-to-noise ratio which compares favorably with that obtained in hyperbolic traps [88,84,10]. Parametric excitation of isolated electron oscillators in such a well characterized environment is ideal for studying collective behaviors, cavity electrodynamics, and fluctuation phenomena.